particles

IMPACT FACTOR 1.7

CITESCORE 3.2

Article

Classical and Bohmian Trajectories in Integrable and Nonintegrable Systems

George Contopoulos and Athanasios C. Tzemos

MDPI

https://doi.org/10.3390/particles7040064 particles

MDPI

Article

Classical and Bohmian Trajectories in Integrable and Nonintegrable Systems

George Contopoulos † and **Athanasios C. Tzemos** *,†

Research Center for Astronomy and Applied Mathematics of the Academy of Athens, Soranou Efessiou 4, GR-11527 Athens, Greece; gcontop@academyofathens.gr
* Correspondence: atzemos@academyofathens.gr
† These authors contributed equally to this work.

Abstract: In the present paper, we study both classical and quantum Hénon–Heiles systems. In particular, we make a comparison between the classical and quantum trajectories of integrable and nonintegrable Hénon–Heiles Hamiltonians. From a classical standpoint, we study both theoretically and numerically the form of invariant curves in the Poincaré surfaces of section for several values of the coupling parameter in the integrable case and compare them with those in the nonintegrable case. Then, we examine the corresponding Bohmian trajectories, and we find that they are chaotic in both cases, but with chaos emerging at different times.

Keywords: chaos; Bohmian quantum mechanics; Born's rule

check for updates

Citation: Contopoulos, G.; Tzemos, A.C. Classical and Bohmian Trajectories in Integrable and Nonintegrable Systems. *Particles* **2024**, 7, 1062–1077. https://doi.org/10.3390/particles7040064

Academic Editor: Armen Sedrakian

Received: 24 September 2024
Revised: 18 November 2024
Accepted: 19 November 2024
Published: 25 November 2024

1. Introduction

A fundamental problem in Quantum Mechanics (QM) concerns the existence of chaotic behaviour in the quantum regime. A classical dynamical system exhibits chaos when it has a bounded phase space and its trajectories are highly sensitive to the initial conditions. However, Standard Quantum Mechanics (SQM) does not predict trajectories for quantum particles. Thus, chaos cannot be defined in the same way as in Classical Mechanics (CM), and most works following SQM rely on studying the quantum properties of the integrable and chaotic classical counterparts. According to the Bohigas–Giannoni–Schmit conjecture [1], the differences between the adjacent eigenvalues of a quantum system corresponding to an integrable classical system follow a Poisson distribution, while the differences between the adjacent eigenvalues of a quantum system corresponding to a nonintegrable classical system follow a Wigner distribution [2–5]. This has been established numerically in various cases. However, this rule may not apply to all cases.

Quantum chaos has been studied in various physical systems: (a) in classically driven chaotic systems, a representative class being the ionized hydrogen atoms inside microwave fields [6,7], (b) in kicked quantum chaotic systems [8], (c) in Bose–Einstein condensates [9–12], (d) in materials where relativistic quantum transport phenomena take place [13,14], (e) in nuclear systems [15], etc.

Bohmian Quantum Mechanics (BQM) is an alternative interpretation of QM that predicts deterministic trajectories for quantum particles, governed by a set of first-order-in-time differential equations, the Bohmian equations [16–19]:

$$m_i\frac{dx_i}{dt}=\hbar Im\left(\frac{\nabla\Psi}{\Psi}\right). \quad (1)$$

where Ψ is the usual wavefunction that satisfies the Schrödinger equation

$$-\frac{\hbar^2}{2m_i}\nabla^2\Psi+V\Psi=i\hbar\frac{\partial\Psi}{\partial t}. \quad (2)$$

BQM is a nonlocal, trajectory-based quantum theory that predicts the same experimental results as Standard QM, provided that the Bohmian particles are distributed according to Born's rule, $P = |\Psi|^2$. The nature and observability of Bohmian trajectories have attracted much interest in the past from both theoretical and experimental standpoints.

In fact, much work has been carried out in recent years on applications of Standard and Bohmian Quantum Mechanics in experimental setups. For example, very important experimental work was performed by Kocsis et al. [20], Braverman and Simon [21] and Foo et al. [22] after the theoretical work of Wiseman on 'weak measurements' [23].

The nonlinear nature of the Bohmian equations (Equation (1)) enables the study of chaotic phenomena at the quantum level using the framework of classical dynamical systems theory, where chaos is characterized by high sensitivity to initial conditions in a bounded phase space. Thus, Bohmian chaos is an open field of research in quantum foundations and has been studied by many authors [24–31]. For a review of our work, see [32], while for an interesting study on the relation between classical chaos and Bohmian Mechanics, see [33].

From the early days of BQM, it was understood that chaos emerges when a Bohmian particle comes close to a nodal point of Ψ (the point where $\Psi = 0$). However, as was shown in [34–36], in the frame of reference of a moving nodal point N, there is a second stagnant point X of the Bohmian flow that is unstable, the so-called 'X-point'. N and X form a nodal point/X-point complex (NPXPC). Whenever a Bohmian trajectory comes close to an NPXPC, it gets scattered by point X, and the local Lyapunov exponent (the so-called 'stretching number') experiences a positive shift [34,35]. The cumulative result of many such close encounters between the trajectory and the NPXPCs is the saturation of the Lyapunov exponent at a positive value, indicating chaos. The NPXPC mechanism describes all the major spikes in the time series of the Lyapunov exponent. However, later, we found that the stagnant points of the Bohmian flow in the inertial frame of reference, the 'Y-points', also produce chaos, but their contribution is, in general, weak [37]. The combined study of X-points and Y-points accounts for the profile of the Lyapunov exponent of a typical Bohmian trajectory. Trajectories that stay away from the X- and Y-points are ordered (thus, their Lyapunov exponent is zero).

To date, most works on Bohmian chaos have focused on systems of noninteracting quantum harmonic oscillators in two dimensions [38]. It is remarkable that, even in the absence of interaction terms in a classical integrable system, its Bohmian counterpart has both chaotic and ordered trajectories. In order to observe Bohmian chaos, one needs, in general, noncommensurable frequencies and an entangled state of the system [26,28,39–41].

Thus, a typical Bohmian system has both ordered and chaotic trajectories, like a classical Hamiltonian system. But Bohmian chaos emerges in a different way than classical Hamiltonian chaos, which is produced by the overlapping of the asymptotic curves of its unstable periodic trajectories [42,43].

In the present paper, we compare, in detail, the ordered and chaotic trajectories of two representative classical systems, one integrable and one nonintegrable, and of the corresponding quantum analogues. As representative systems, we have chosen two cases of interacting oscillators with coordinates x and y and with equal angular frequencies along the x- and y-coordinates ($\omega_x = \omega_y = 1$), described by the Hénon–Heiles Hamiltonians

$$H = \frac{1}{2}(x^2 + y^2 + \dot{x}^2 + \dot{y}^2) + \epsilon\left(xy^2 \pm \frac{x^3}{3}\right). \tag{3}$$

The corresponding velocities are $\dot{x}$ and $\dot{y}$, while ϵ is the coupling strength parameter. When the sign of $\frac{x^3}{3}$ is negative, we have the original Hénon–Heiles system, which is nonintegrable. Conversely, the positive sign refers to a case where a second integral of motion exists and the system is integrable [44].

The Hénon–Heiles Hamiltonian has been one of the most well-studied systems in the theory of classical chaos due to its simple form and its high complexity as regards the corresponding trajectories [45–48]. Thus, it has been used as a standard system for studying the signatures of classical chaos in the physical properties of the corresponding quantum systems. Moreover, several variations of the Hénon–Heiles model have been used extensively in the field of chemical physics in order to understand vibrational modes in molecular systems [49–51]. However, only a few works have been conducted from a Bohmian standpoint [52–54].

The structure of the present paper is the following: In Section 2.1, we discuss the classically integrable quantum Hénon–Heiles system. We find the invariant curves of the trajectories of the classical system. This system, of course, has no chaos. But, in the corresponding quantum system (Section 2.2), most trajectories are chaotic (except if $\epsilon = 0$), although their chaotic behaviour becomes apparent only after a rather long time. Then, we find the eigenvalues of the chaotic system, the differences between successive eigenvalues and the statistics of these differences. These statistics can be approximated by a Poisson distribution (and not a Wigner distribution).

In Section 3, we perform the same work for the nonintegrable Hénon–Heiles system. In this case, there is both order and chaos in the classical system (Section 3.1). Then, in Section 3.2, we study the corresponding Bohmian system. We calculate its eigenvalues and their differences. The statistics of these differences are again approximated by a Poisson distribution and not by a Wigner distribution. Finally, we find the remarkable result that the times needed for chaos to emerge are much shorter in the Bohmian case corresponding to the integrable classical system than in the nonintegrable system.

In Section 4, we make a comparison between the two cases and draw our conclusions.

2. Integrable Hénon–Heiles Hamiltonian

2.1. Classical Case

The integrable classical Hénon–Heiles Hamiltonian system is described by the following Hamiltonian:

$$H = \frac{1}{2}(\dot{x}^2 + \dot{y}^2 + x^2 + y^2) + \epsilon\left(xy^2 + \frac{x^3}{3}\right) = E. \tag{4}$$

It differs from the usual Hénon–Heiles Hamiltonian only in the sign of the cubic term (+ instead of $-$). The corresponding second integral of motion is [44]

$$Q = \dot{x}\dot{y} + xy + \epsilon\left(yx^2 + \frac{y^3}{3}\right) = K. \tag{5}$$

The invariant curves for $y = 0$ are given by

$$\dot{x}\dot{y} = K, \tag{6}$$

and hence, $\dot{y} = K/\dot{x}$, and Equation (5) gives

$$f \equiv \dot{x}^4 + \left(x^2 + 2\frac{\epsilon x^3}{3} - 2E\right)\dot{x}^2 + K^2 = 0. \tag{7}$$

Its solution is

$$\dot{x}^2 = \frac{1}{2}\left(2E - x^2 - 2\frac{\epsilon x^3}{3} \pm \sqrt{\left(2E - x^2 - \frac{2\epsilon x^3}{3}\right)^2 - 4K^2}\right). \tag{8}$$

In the numerical examples, we set $E = 1$, and for any given ϵ, we have invariant curves for various values of K (Figure 1a–d). If we fix a different value of E, then we find similar results.

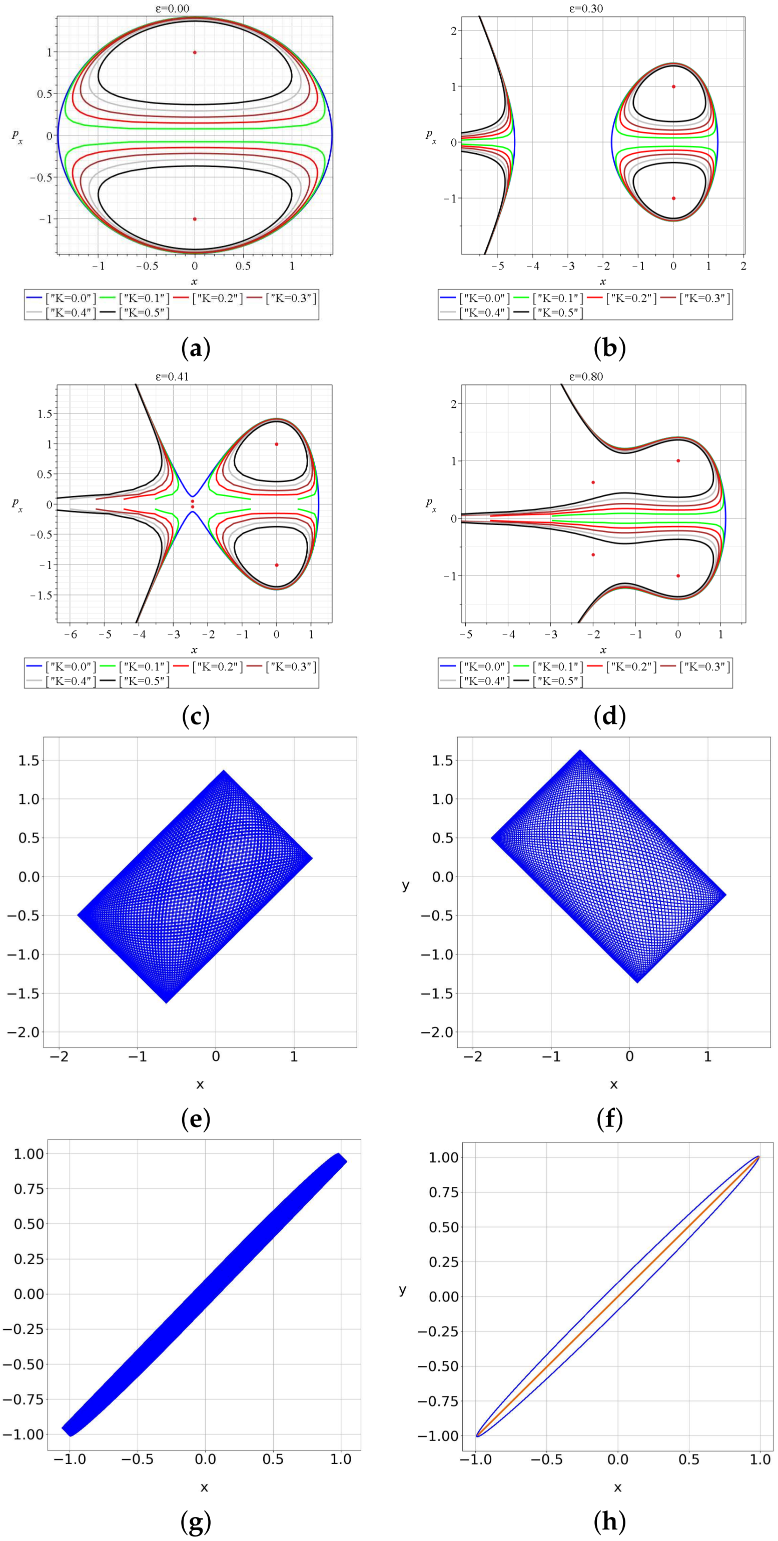

(**a**) (**b**) (**c**) (**d**) (**e**) (**f**) (**g**) (**h**)

Figure 1. (**a**–**d**): Invariant curves for different values of the interaction term ϵ in the integrable case for $E = 1$. The different colours correspond to various values of the second integral K. In all cases, $y = 0$. (**a**) $\epsilon = 0$, (**b**) $\epsilon = 0.3$, (**c**) $\epsilon = 0.41$ and (**d**) $\epsilon = 0.8$. The red dots correspond to the periodic orbits, stable or unstable. Then, we show the main types of non-escaping classical orbits with (**e**) $x(0) = 0.1, y(0) = 0.2, \dot{x}(0) = -0.2768, \dot{y}(0) = -1.3678, \epsilon = 0.3, K = 0.4$; (**f**) $x(0) = 0.1, y(0) = 0.2, \dot{x}(0) = 0.3097, \dot{y}(0) = -1.3607, \epsilon = 0.3, K = -0.4$; (**g**) $x(0) = 0.1, y(0) = 0.2, \dot{x}(0) = \dot{y}(0) = 0.9874, \epsilon = 0.01, K = 0.995$; and (**h**) $\epsilon = 0, x(0) = 0.1, y(0) = 0.2, \dot{x}(0) = \dot{y}(0) = 0.9874, K = 0.9949$ (blue) and $\epsilon = 0, x(0) = y(0) = 0, \dot{x}(0) = \dot{y}(0) = 1, K = 1$ (red).

The outermost invariant curve (for $E = 1$ and $K = 0$) is given by

$$\dot{x}^2 = 2 - x^2 - \frac{2\epsilon x^3}{3}. \tag{9}$$

We also have the solution $\dot{x}^2 = 0$.

For $\epsilon = 0$, the outermost invariant curve is a circle $\dot{x}^2 + x^2 = 2$ and the axis $\dot{x} = 0$. Inside this circle, we have invariant curves above and below the axis $\dot{x} = 0$. For $K > 0$, the invariant curves are

$$\dot{x}^2 = \frac{1}{2}\left(2 - x^2 \pm \sqrt{(2 - x^2)^2 - 4K^2}\right). \tag{10}$$

For $x = 0$ and $\epsilon = 0$, we have the maxima and minima $\dot{x}^2$, with $\dot{x}^2 = 1 \pm \sqrt{1 - K^2}$. As ϵ increases from $\epsilon = 0$ (Figure 1a), the circle is distorted, and we also have a second set of invariant curves on the left that go to minus infinity (Figure 1b). If

$$\frac{\partial f}{\partial x} = \frac{\partial f}{\partial \dot{x}} = 0, \tag{11}$$

then we have periodic trajectories. For $E = 1$, we find

$$\frac{\partial f}{\partial \dot{x}} = 2\dot{x}\left[2\dot{x}^2 + x^2 + \frac{2\epsilon x^3}{3} - 2\right] = 0, \tag{12}$$

$$\frac{\partial f}{\partial x} = 2\dot{x}^2[x + \epsilon x^2] = 0. \tag{13}$$

One solution is

$$x = 0, \dot{x}^2 = 1. \tag{14}$$

This gives two stable periodic trajectories at the centres above and below the origin with $K = 1$. The invariant curves for K between 0 and 1 surround the unstable points $x = 0$, $\dot{x} = \pm 1$.

There are also escapes along the y-axis. In Figure 1a,b, such orbits appear close to the points $(x = 0, \dot{x}\pm = 1)$ when $\epsilon > \frac{1}{2\sqrt{3}} \simeq 0.289$.

Another solution is

$$x = -\frac{1}{\epsilon}, \qquad \dot{x}^2 = 1 - \frac{1}{6\epsilon^2}. \tag{15}$$

This gives two unstable trajectories above and below the x-axis with $K = 1 - \frac{1}{6\epsilon^2}$, which exist when $\epsilon \geq \frac{1}{\sqrt{6}}$. The value $\epsilon = \epsilon_{esc} = \frac{1}{\sqrt{6}}$ is the escape perturbation. The invariant curves with K between 0 and $1 - \frac{1}{6\epsilon^2}$ extend to minus infinity close to the $x = 0$ axis and, above the upper periodic point or below the lower invariant point, surround (from the right) the stable periodic points. The invariant curves with K between $1 - \frac{1}{6\epsilon^2}$ and 1 form loops around the stable periodic points.

As ϵ increases from $\epsilon = 0$, the second set of invariant curves approaches the main set (around (0,0)), and for $\epsilon = \frac{1}{\sqrt{6}} \simeq 0.408$, the outermost invariant curves reach each other at a singular point $\dot{x} = 0, x = -2.449$.

For $\epsilon = 0.8$, we have two unstable trajectories at $x = -2$ and $x = \pm\frac{1}{3}$ (Figure 1d). For $K > 1$, there are invariant curves only at the left of $x = -\frac{1}{\epsilon}$. The corresponding trajectories are, in general, Lissajous figures with axes parallel to the diagonals $x = \pm y$ (Figure 1e,f).

Theoretically, the boundaries of these figures are given by eliminating $\dot{x}$ and $\dot{y}$ from Equations (4) and (5) of the integrals of motion H and Q and the relation [55]

$$J = \frac{\partial Q}{\partial \dot{x}}\dot{y} - \frac{\partial Q}{\partial \dot{y}}\dot{x} = 0. \tag{16}$$

This relation gives

$$\dot{y}^2 - \dot{x}^2 = 0 \rightarrow \dot{x} = \pm\dot{y}. \tag{17}$$

Introducing these values into Equations (2) and (3), we find, for $E = 1$,

$$\dot{x}^2 = 1 - \frac{1}{2}(x^2 + y^2) - \epsilon\left(xy^2 + \frac{x^3}{3}\right) = \pm\left[K - xy - \epsilon\left(x^2 y + \frac{y^3}{3}\right)\right]. \tag{18}$$

This equation for x, y can be written in the form

$$(x \mp y)^2 + \frac{2\epsilon}{3}(x \mp y)^3 = 2 \mp 2K. \tag{19}$$

The solutions give two straight lines parallel to the diagonal $x = y$ at distances depending on $(1 - K)$ and two straight lines parallel to the diagonal $x = -y$ depending on the value of $(1 + K)$. Thus, in general, the Lissajous figures are elongated (Figure 1g). In the particular case of $\epsilon = 0$, all the trajectories are periodic, forming ovals or, in the limiting cases $1 \mp K = 0$, straight lines (Figure 1h).

2.2. Quantum Case

The Schrödinger Equation (2) with $V = V_0 + V_p = \frac{1}{2}(x^2 + y^2) + \epsilon(xy^2 \pm x^3/3)$ is not analytically solvable. However, we can follow the standard procedure [56] of the direct diagonalization of the perturbed Hamiltonian, exploiting the fact that the unperturbed system is analytically solvable, and thus, its eigenstates for a complete basis $\{|\Phi_l\rangle\}$ in the Hilbert space. The eigenstates are $|\Phi_1\rangle = |0\rangle_x \otimes |0\rangle_y \equiv |00\rangle$, $|\Phi_2\rangle = |01\rangle$, $|\Phi_3\rangle = |10\rangle, \Phi_4 = |02\rangle \ldots$ where $|0\rangle, |1\rangle \ldots$ correspond to the energy eigenstates of the two quantum harmonic oscillators in the x- or y-direction. Following this procedure, the Hamiltonian operator in the basis $\Phi_l\rangle$ becomes a matrix, whose arbitrary element is written as

$$H_{i,j} = \int_{-\infty}^{\infty}\int_{-\infty}^{\infty} \Phi_i^{\dagger}(H_0 + V)\Phi_j dxdy. \tag{20}$$

The diagonalization of the Hamiltonian matrix of the perturbed system gives the corresponding eigenvalues and eigenvectors. Then, it is straightforward to calculate the spacings between energy levels.

The eigenvectors of the perturbed system can then be written as linear combinations of the eigenstates of the unperturbed system, i.e.,

$$|\tilde{\Phi}_r\rangle = \sum_l c_{lr}|\Phi_l\rangle. \tag{21}$$

Thus, an initial wavefunction $|\Psi_0\rangle = |\Psi(t = 0)\rangle$ leads to

$$|\Psi(t)\rangle = \sum_r \exp(-i\tilde{E}_r t/\hbar)\langle\tilde{\Phi}_r|\Psi_0\rangle|\tilde{\Phi}_r\rangle = \sum_{l,l',r} c^*_{l'r} c_{lr} \exp(-i/\hbar\tilde{E}_r t)\langle\Phi_{l'}|\Psi_0\rangle|\Phi_l\rangle. \tag{22}$$

We start with a wavefunction that has, in the position representation, the form

$$\Psi_0 = a\Psi_{0,0} + b\Psi_{1,0} + c\Psi_{1,1}, \tag{23}$$

where $\Psi_{m,n} \equiv \Psi_m(x)\Psi_n(y)$ and $\Psi_m(x), \Psi_n(y)$ are the 1-D energy eigenstates of the oscillators [56] in x- and y-coordinates, respectively, i.e.,

$$\Psi_{m,n}(x, y, t) = \prod_{q=x}^{y} N_q \exp\left(-\frac{\omega_q q^2}{2\hbar}\right) \exp\left(-\frac{i}{\hbar}E_s t\right) H_s\left(\sqrt{\frac{M_q\omega_q}{\hbar}}q\right), \tag{24}$$

and we set $a = b = c = 1/\sqrt{3}$ (thus, $a^2 + b^2 + c^2 = 1$). Moreover, $s = m, n$ are integers for x and y, while H_s represents Hermite polynomials of order s. N_q is the normalization constant $N_q = \frac{(M_q\omega_q)^{\frac{1}{4}}}{\pi\hbar\sqrt{2^s s!}}$, and the energy corresponding to the term $\Psi_{m,n}$ is

$$E_{m,n} = E_m + E_n = \left(\frac{1}{2} + m\right)\hbar\omega_x + \left(\frac{1}{2} + n\right)\hbar\omega_y. \tag{25}$$

We work with $\omega_x = \omega_y = M_x = M_y = \hbar = 1$.

The wavefunction (23) is the most well-studied in the field of Bohmian chaos [39], since it has the simplest form that can exhibit chaos [28].

We note that, due to the common frequencies, the unperturbed problem has a degeneracy: i.e., for a given value $n = n_x + n_y$, there are $n + 1$ states with equal energies. This degeneracy is lifted by the term $\epsilon(xy^2 + x^3/3)$. The number of states $|\Phi_l\rangle$ is truncated at a high level depending on ϵ. The first 45 eigenvalues for $\epsilon = 0.05$ are given in Figure 2a. The differences between the successive eigenvalues with the same sum $n = n_x + n_y$ are very small (the same level), while those between successive levels are large (Figure 2b). In this case ($\epsilon = 0.05$), it is sufficient to take N up to $N = 45$ because the coefficients of the higher-order terms are very small. However, for larger values of the interaction parameter ϵ, we need a much larger number of energy levels in our truncation.

For example, in the case of $\epsilon = 0.2$, it is sufficient to take a much larger number $N = 136$ (Figure 2). If we calculate the differences between the successive energy levels of a given truncation, then we can count how many times we find a value s in our ensemble. Such a histogram is given in Figure 2c. There, we see that the distribution of the energy gaps is similar to a Poisson distribution (see also the Conclusions Section) of the form

$$f(s) \propto \exp(-s), \tag{26}$$

where f is the proportion of the distances s between adjacent energy levels.

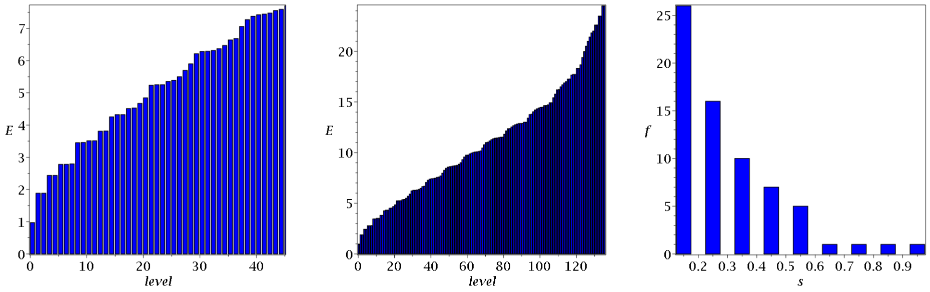

(**a**) (**b**) (**c**)

Figure 2. (**a**) The distributions of the first 45 and (**b**) of the first 136 energy levels in the integrable case when $\epsilon = 0.2$. (**c**) A histogram of the (135) successive energy gaps of value s.

Since the initial wavefunction for $\omega_x = \omega_y = 1$ gives $E_{0,0} = 1, E_{1,0} = 2, E_{1,1} = 3$, the total energy is $\langle E\rangle = a^2E_{0,0} + b^2E_{1,0} + c^2E_{1,1} = 2$, and thus, the average energy is $E_{av} = 2$. For $\epsilon > 0$, the average energy is larger than 2 and increases with ϵ (see the last section).

The Bohmian trajectories in this case are, in general, chaotic. This is due to the fact that the trajectories approach the moving nodal points and are deviated by their nearby X-points according to the NPXPC mechanism [34,35].

This fact, however, is not obvious. In a previous paper [57], we considered the resonant case of a two-qubit system of the unperturbed 2d harmonic oscillator, where we have, in general, infinite nodal points along a straight line. In that paper, we found that when the frequencies ω_x, ω_y of the unperturbed potential $V = \frac{1}{2}(\omega_x^2x^2 + \omega_y^2y^2)$ are commensurable, then all the corresponding Bohmian trajectories are periodic. In particular, when $\omega_x = \omega_y$, there are no nodal points at all (the analytical formulae for the positions of the nodal points have a denominator $\sin[(\omega_x - \omega_y)t]$ that becomes zero at $\omega_x = \omega_y$; i.e., the nodal points are at infinity.

In the present case, we have the same resonance $\omega_x = \omega_y = 1$. However, in the quantum Hénon–Heiles problem, the positions of the nodal points have no specific form in the configuration space due to the anisotropy in the x- and y-coordinates. Specifically, the nodal points enter the central region of the support of the wavefunction in a complex way and scatter the incoming Bohmian trajectories.

In Figure 3a, we calculate a Bohmian trajectory up to $t = 4\pi$ for $\epsilon = 0.05$. If this trajectory were periodic, it would return to its initial point after every $\Delta t = 2\pi$. This does not happen in the present case. Therefore, the trajectory is not periodic. The same trajectory was then integrated (for $\epsilon = 0.05$) up to $t = 2\pi \times 10^3$. This is chaotic (Figure 3b), as was verified by calculating the Lyapunov characteristic number. Its corresponding 'colour plot', which shows the number of times a trajectory passes through every bin of area 0.05×0.05 in the configuration space up to $t = 2\pi \times 10^5$, is shown in Figure 3c. We see that the Bohmian trajectories are very different from the classical trajectories. They approach some nodal points from time to time, and they become chaotic in the long run. In fact, they require some time to exhibit their chaotic character, with the amount of time depending on the value of the perturbation parameter ϵ.

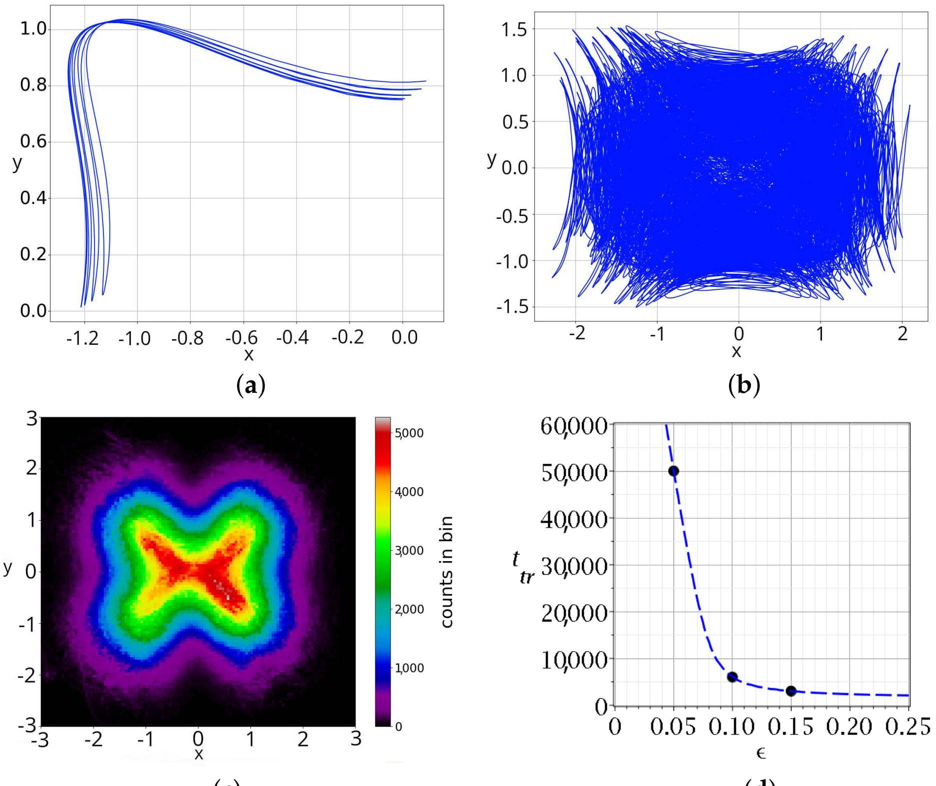

(**a**) (**b**) (**c**) (**d**)

Figure 3. (**a**) A Bohmian trajectory ($x(0) = 0, y(0) = 0.75$) for $\epsilon = 0.05$ up to a) $t = 4\pi$ and (**b**) $t = 10^3 \times 2\pi$. In (**c**), we give the long limit distribution of the points of this trajectory up to $t = 10^5 \times 2\pi$. It is a chaotic-ergodic trajectory. Finally, in (**d**), we show the time needed for about 98% of the trajectories, produced by 5×10^3 Born-distributed initial conditions, to show their chaotic character for various values of ϵ (integrable case).

The manifestation of chaoticity occurs when the Bohmian trajectories cover practically all available support of the wavefunction [58,59]. Specifically, Bohmian particles, after the approach of a nodal point, change their apparently ordered form and extend to larger distances, showing their chaotic character. The transition time t_{tr} required for most trajectories (about 98% in an ensemble of 5×10^3 Born-distributed initial conditions) to show their chaotic character is given for some values of ϵ in Figure 3d.

If the perturbation ϵ is large, the time of manifestation of chaoticity is short, but as ϵ decreases, this time increases and becomes very large for small ϵ, tending to infinity as $\epsilon \to 0$. This behaviour is similar to that already observed for noncommensurable frequencies [60].

3. Nonintegrable Hénon–Heiles Hamiltonian

3.1. Classical Case

The nonintegrable Hénon–Heiles Hamiltonian is

$$H = H_0 + \epsilon H_1 = \frac{1}{2}(\dot{x}^2 + \dot{y}^2 + x^2 + y^2) + \epsilon\left(xy^2 - \frac{x^3}{3}\right) = E, \tag{27}$$

which has both ordered and chaotic trajectories.

Hénon and Heiles [45,46] gave Poincaré surfaces of section for $\epsilon = 1$ and various values of energy E. Here, however, we will fix $E = 1$ (as in Section 2) and give surfaces of section ($y = 0, \dot{y} > 0$) for various values of ϵ that are characteristic of the onset of chaos, as well as the introduction of escapes to infinity (Figure 4a–f). For small values of ϵ, chaos is insignificant, but beyond $\epsilon = 0.3$, chaos increases and becomes dominant (Figure 4b–d). Furthermore, there is a second set of invariant curves on the right that extend to + infinity. As ϵ increases, this set approaches the central set of invariant curves, and for $\epsilon_{crit} = 0.4$, it joins it. The value $\epsilon = \epsilon_{crit} = 0.408$ is the escape perturbation. With larger ϵ, most trajectories escape to infinity. However, there remain some small islands of stability (Figure 4f).

In Figure 4a,b, we see two main islands of stability around two stable points on the x-axis that belong to stable periodic trajectories. Between them, there is an unstable periodic orbit and chaos, as seen around it for $\epsilon \geq 0.3$ (Figure 4b). But, in Figure 4c,d, we see many more islands of stability and, between them, unstable points and some small regions of chaos. The stable points on the left and on the right of Figure 4a–c have become unstable in Figure 4d. In Figure 4d,f, several chaotic regions overlap, and chaos becomes important.

In Figure 4e, we see that beyond the right limit of Figure 4d, there is one more set of invariant curves that extend to ∞. As ϵ increases further to $\epsilon = 0.409$, this set joins the outermost invariant curve around the centre, and most chaotic trajectories escape to infinity on the right (Figure 4f).

The proportion of chaotic trajectories as a function of ϵ is given in Figure 4g. For small ϵ, this gives the chaotic area divided by the total area of the surface of section. We see that chaos is insignificant for ϵ up to $\epsilon = 0.3$, but then it increases abruptly and reaches 92% at the escape perturbation. Beyond the escape perturbation, there remain some islands of stability that decrease gradually as ϵ increases.

The forms of the classical trajectories are shown in Figure 5. There are trajectories forming rings around the stable periodic trajectories of Figure 4 on the right and on the left of the origin (Figure 5a,b), trajectories around the stable trajectory at $x = 0$ and $\dot{x} > 0$ (Figure 5c) (and a similar trajectory for $\dot{x} < 0$), as well as many chaotic trajectories, like the one shown in Figure 5d. There are also small regions of trajectories around stable periodic trajectories of higher periods.

These trajectories are very different from those of the integrable classical case (Figure 1e–h), except for the trajectories in Figure 5c above and below the centre of Figure 4c, which are similar to the elongated Lissajous curve of Figure 1g.

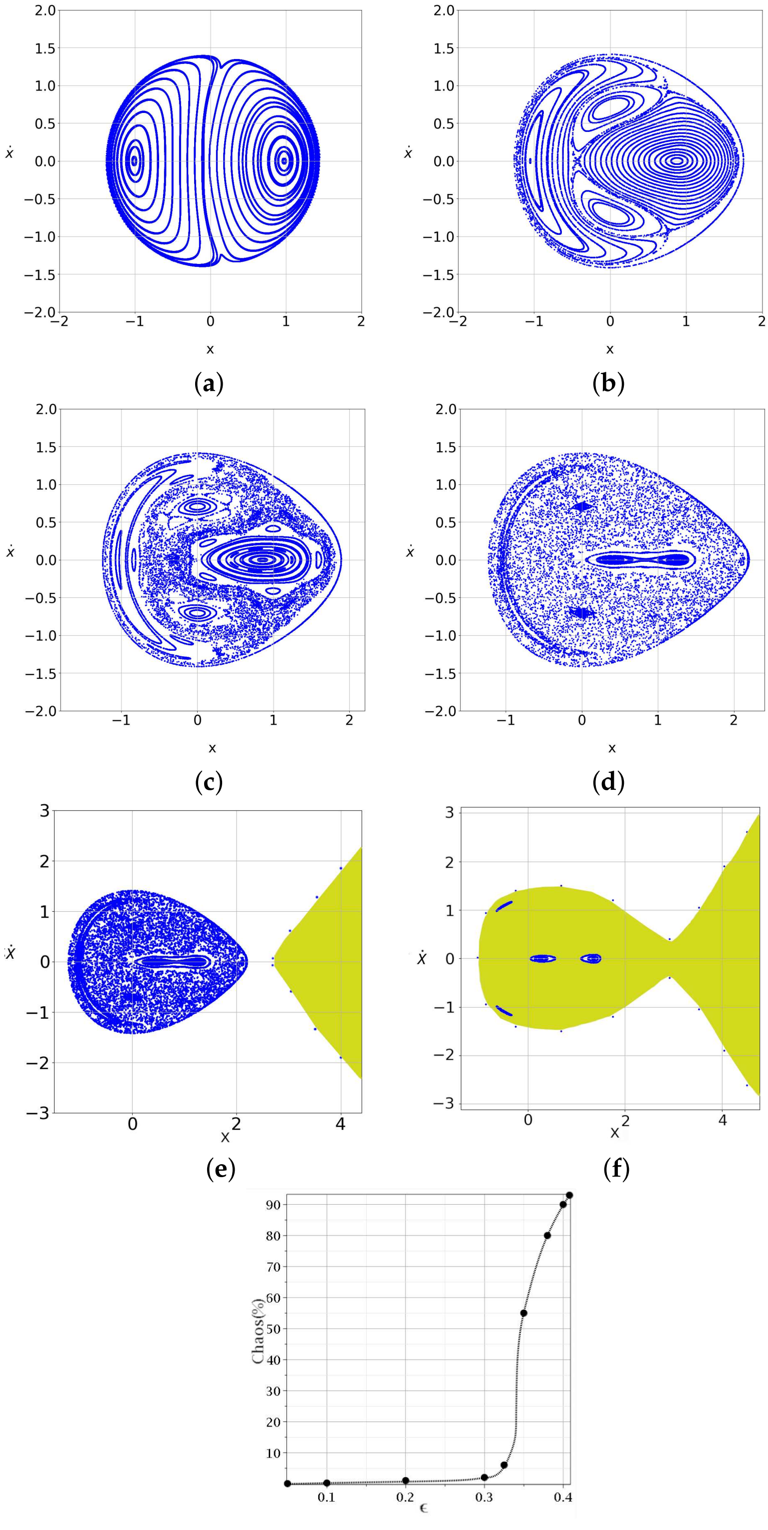

(**a**) (**b**) (**c**) (**d**) (**e**) (**f**) (**g**)

Figure 4. Poincaré surfaces of section $y = 0, \dot{y} > 0$ of the classical nonintegrable system for a fixed value of energy $E = 1$ and for certain characteristic values of the coupling constant ϵ that show the emergence of chaos and the introduction of escapes to infinity. (**a**) $\epsilon = 0.05$, (**b**) $\epsilon = 0.3$, (**c**) $\epsilon = 0.35$. (**d**,**e**) refer to the same perturbation $\epsilon = 0.4$, while (**f**) refers to $\epsilon = 0.409$. The region of escaping trajectories is coloured yellow. In (**g**), we show the proportion of chaotic orbits in the Poincaré surface of section as a function of ϵ.

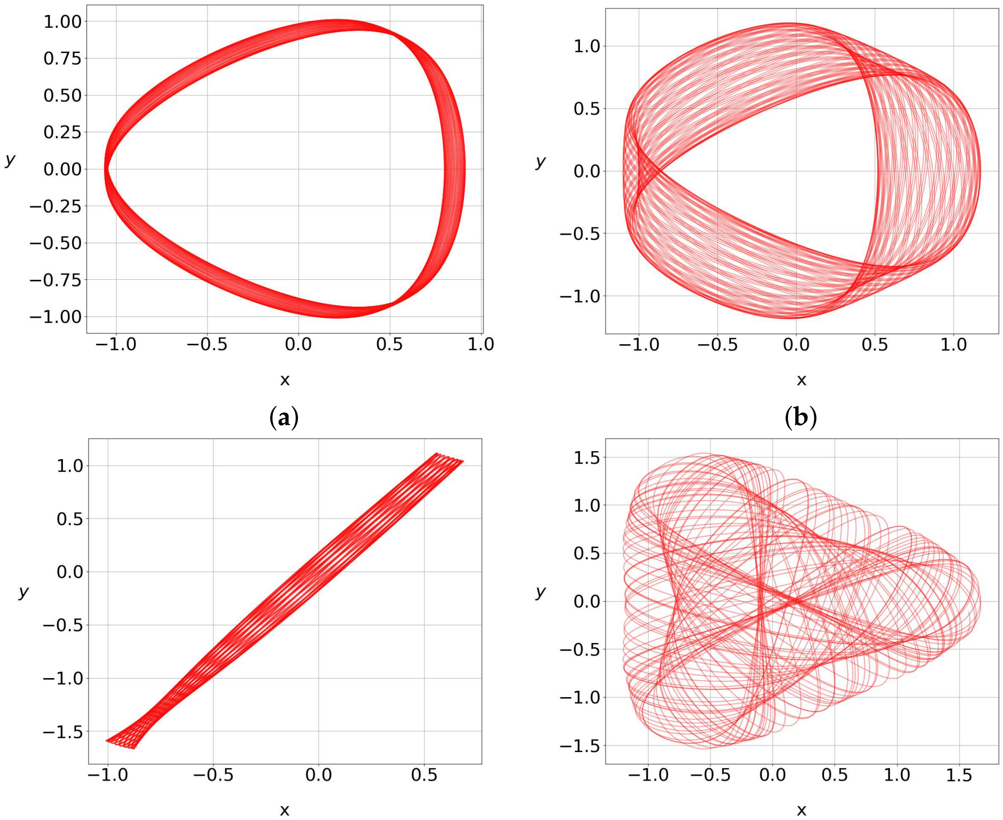

(**a**) (**b**)

(**c**) (**d**)

Figure 5. Four trajectories around the Poincaré surface of section corresponding to $\epsilon = 0.35$ and $E = 1$: (**a**) $x(0) = 0.8, y(0) = 0, \dot{x}(0) = 0, \dot{y}(0) = 1.2163$; (**b**) $x(0) = -1, y(0) = 0, \dot{x}(0) = 0, \dot{y}(0) = 0.8756$; (**c**) $x(0) = 0, y(0) = 0, \dot{x}(0) = 0.75, \dot{y}(0) = 1.19896$; and (**d**) $x(0) = -0.1, y(0) = 0, \dot{x}(0) = 0$, $\dot{y}(0) = 1.41059$. The last one is chaotic.

3.2. Quantum Case

The Bohmian quantum analogue of the nonintegrable Hénon–Heiles system is very similar to the corresponding integrable case for the same value of energy $E = 1$. We work with the same wavefunction as in the integrable case. The corresponding average energies E_{av} for increasing values of ϵ are shown in the Conclusions Section.

In Figure 6a, we show the eigenvalues of this case, which are very similar to those of the integrable case in Figure 2a,b. Figure 6b gives the distribution of the differences between adjacent eigenvalues, which is similar to that in Figure 2c for the integrable case.

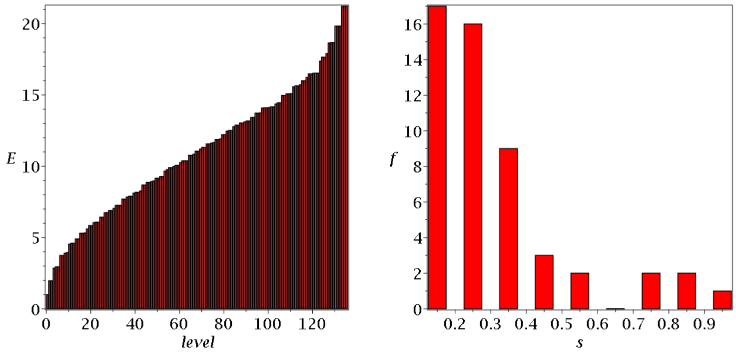

(**a**) (**b**)

Figure 6. (**a**) The distribution of the first 136 energy levels in the nonintegrable case when $\epsilon = 0.2$. (**b**) A histogram of the (135) successive energy gaps of value s.

Figure 7 shows a chaotic Bohmian trajectory for $\epsilon = 0.05$ and times (a) $t = 4\pi$ and (b) $t = 2\pi \times 10^3$. Figure 7c is the colour plot of this trajectory for a long time ($t = 2\pi \times 10^5$). These trajectories are similar to those of the integrable case (Figure 3a–c). Finally, Figure 7d gives the time needed for the trajectories of different ϵ to show their chaotic character, and this is to be compared with Figure 3d. The chaotic character time is larger for smaller ϵ and tends to infinity as $\epsilon \to 0$. However, the times for the establishment of chaoticity are much larger in the nonintegrable case.

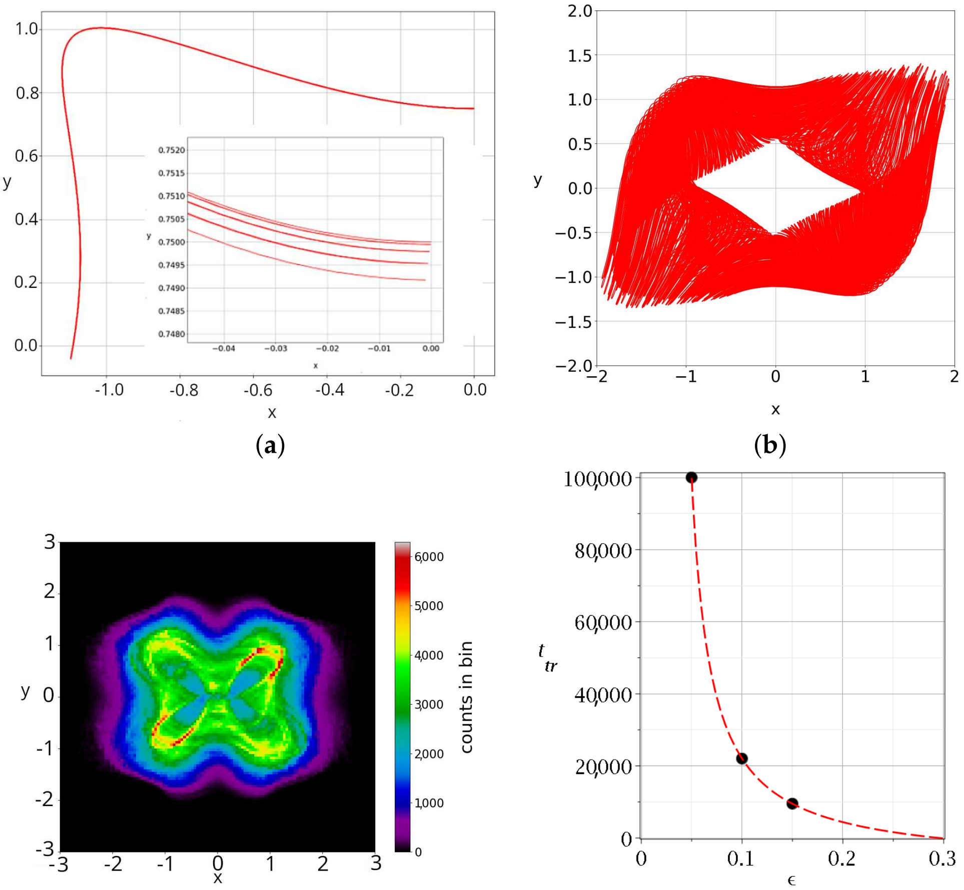

(**a**) (**b**)

(**c**) (**d**)

Figure 7. (**a**) The Bohmian trajectory of the same initial condition as in Figure 3 for $\epsilon = 0.05$: (**a**) up to $t = 4\pi$ (in the inset, we show a zoomed-in view of part of the trajectory in Figure 7a, where we see that it is not periodic), (**b**) up to time $t = 10^3 \times 2\pi$ and (**c**) the colour plot of the long limit distribution of its points for $t = 2\pi \times 10^5$. It is a chaotic-ergodic trajectory ($x(0) = 0, y(0) = 0.75$). (**d**) The times needed for about 98% of the trajectories, produced by 5×10^3 Born-distributed initial conditions, to show their chaotic character for various values of ϵ (nonintegrable case).

4. Conclusions

In this paper, we studied the classically integrable and nonintegrable Hénon–Heiles systems from both classical and Bohmian quantum perspectives.

(A) In the Bohmian approach, the integrable and nonintegrable systems are similar in several ways:

1. The distributions of the eigenvalues of both integrable and nonintegrable systems are very similar (Figure 8a).
2. The energy differences s between successive eigenvalues are similar. In Figure 8b, we compare the distributions of s in the integrable and nonintegrable cases (Figures 2c and 6b). In both cases, we have a Poisson distribution of the form $P(\bar{s}) \propto \exp(-\bar{s})$, where $\bar{s} = s/s_{av}$ (s_{av} is the average s) is the normalized gap between successive energy

levels. Notably, the Wigner function is not computable in the nonintegrable case of the Hénon–Heiles system, contrary to the common belief that the distribution of the differences ΔE between adjacent eigenvalues has a Wigner form when the classical system is chaotic (while it has a Poissonian form in the integrable cases). In fact, we find the same behaviour even for $\epsilon = 0.35$, where the classical system has a significant amount of chaos (Figure 4c). However, further work is needed in order to find whether this unexpected result is also valid in other cases with more complex Hamiltonians.

3. In Figure 8c, we compare the average energies of the two systems for the same values of ϵ. The average energies start at $E_{av} = 2$ for $\epsilon = 0$ and increase as ϵ increases. However, the increase is much slower in the nonintegrable case. The reason seems to be the following: the perturbation of the integrable case $\epsilon(xy^2 + x^3/3)$ is much larger than the perturbation $\epsilon(xy^2 - x^3/3)$ of the nonintegrable case for the same ϵ.
4. The Bohmian trajectories are, in general, chaotic if $\epsilon \neq 0$ in both integrable and nonintegrable cases. The chaotic character of the trajectories takes more time to be established as the perturbation parameter decreases (Figure 8d). This time tends to infinity when $\epsilon \to 0$. However, the times for the same ϵ are larger in the nonintegrable case.
5. The colour plots (Figures 3c and 7c) are similar.

Therefore, the Bohmian effects in both cases are similar, but stronger in the integrable case.

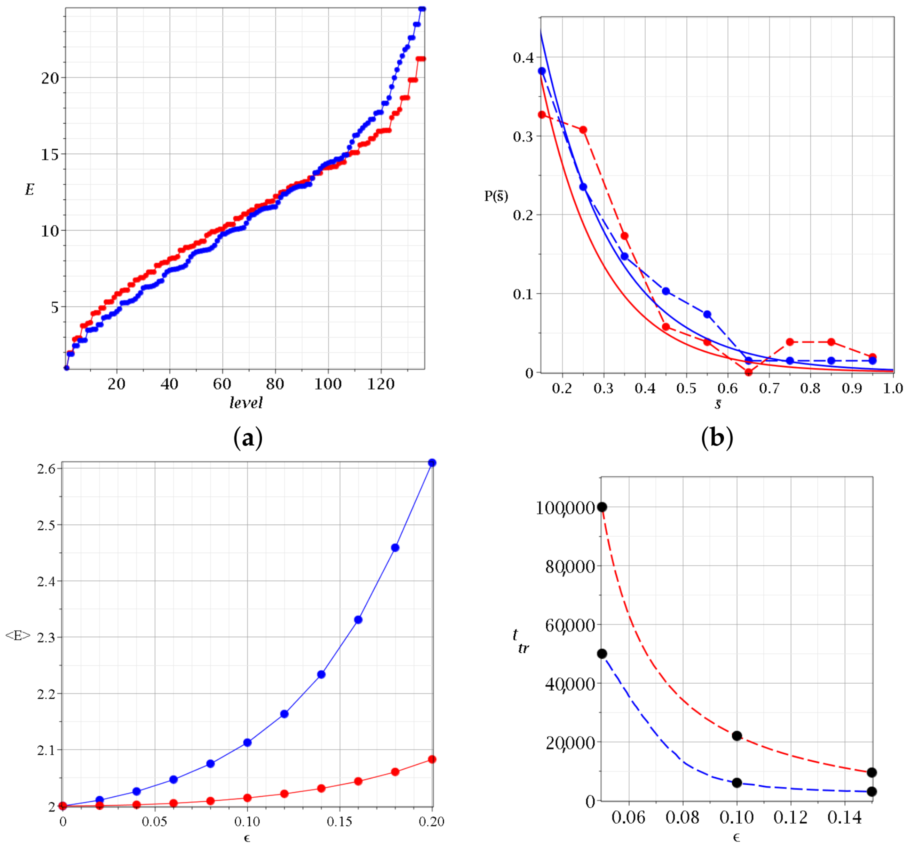

(**a**) (**b**)

(**c**) (**d**)

Figure 8. (**a**) The distribution of the energy levels of the integrable (blue) and nonintegrable (red) cases and (**b**) the probability of finding certain values for the spacings between successive energy levels when $\epsilon = 0.2$. The solid lines are Poisson functions fitting the two observed distributions (dashed lines). We observe that the Poisson functions are very similar to each other. (**c**) The average energy up to t = 10,000 as a function of ϵ. A larger ϵ leads to a larger $\langle E \rangle$. (**d**) The critical time when the majority of trajectories (about 98% in a realization of Born's rule distribution containing 5×10^3 initial conditions) exhibit chaos as a function of ϵ. It is remarkable that in the integrable case (blue curve), Bohmian chaos emerges faster than in the nonintegrable case (red curve).

(B) In the classical approach, we calculate the invariant curves for various values of ϵ.

1. In the integrable case, the invariant curves form closed loops above and below the origin around two stable points. But, with ϵ above an escape value ϵ_{crit}, the invariant curves starting close to the x-axis escape to the left, to minus infinity, also surrounding the closed invariant curves above or below the origin $(0,0)$. In the nonintegrable case, there are closed invariant curves on the left and on the right of the origin, but there are also islands of stability that are symmetric with respect to the x-axis. If ϵ is larger than the escape value ϵ_{esc}, most trajectories (but not all) escape to the right to infinity.
2. However, the main difference between the two systems is the appearance of chaos in the nonintegrable case. The proportion of chaotic trajectories is very small up to a critical value ϵ_{cr}, and for larger ϵ, it increases abruptly. Beyond the escape perturbation ϵ_{esc}, there are only some small islands of stability that decrease gradually as ϵ increases further.
3. In the integrable cases, the non-escaping classical trajectories are, in general, Lissajous figures with axes parallel to the diagonals $y = \pm x$. In the limiting case $\epsilon = 0$, the trajectories are closed loops or straight lines. The classical trajectories in the nonintegrable Hénon–Heiles case are either ordered, surrounding, in every case, a stable periodic trajectory, or chaotic. For example, there are trajectories forming rings around the stable points with $y = 0$ and $\dot{x} = 0$. But, if ϵ is larger than the escape perturbation ϵ_{crit}, most classical trajectories escape to infinity.

Our main conclusion is that the Bohmian trajectories are chaotic, in general, in both the integrable and nonintegrable cases. These results are important for the field of Bohmian chaos, which has been mainly developed by studying entangled wavefunctions of two noninteracting quantum harmonic oscillators. There, it was found that both ordered and chaotic trajectories coexist. However, as with the case ϵxy^2 that we studied in [60], we find that the interaction leads to the dominance of chaotic Bohmian trajectories in the course of time. Thus, it is reasonable to expect that chaos is dominant in more general Hamiltonians.

The study of closed quantum systems with interacting parts is an important and necessary step before moving to the much more complicated, but also realistic, case of open quantum systems, where the environmental interaction induces new effects, such as decoherence and dissipation [61–63].

Author Contributions: Conceptualization, G.C. and A.C.T.; methodology, G.C. and A.C.T.; formal analysis, G.C. and A.C.T.; investigation, G.C. and A.C.T.; writing—original draft, G.C.; visualization, A.C.T.; supervision, G.C. All authors have read and agreed to the published version of the manuscript.

Funding: This research received no external funding.

Data Availability Statement: The datasets generated during the current study are available from the corresponding author upon reasonable request.

Acknowledgments: This research was conducted in the framework of the programme of the Research Committee of the Academy of Athens, "Study of order and chaos in quantum dynamical systems". (No. 200/1026).

Conflicts of Interest: The authors declare no conflict of interest.

References

1. Bohigas, O.; Giannoni, M.J.; Schmit, C. Characterization of chaotic quantum spectra and universality of level fluctuation laws. *Phys. Rev. Lett.* **1984**, *52*, 1. [CrossRef]
2. Haake, F. *Quantum Signatures of Chaos*; Springer: Boston, MA, USA, 1991.
3. Gutzwiller, M.C. *Chaos in Classical and Quantum Mechanics*; Springer Science & Business Media: New York, NY, USA, 2013; Volume 1.
4. Wimberger, S. *Nonlinear Dynamics and Quantum Chaos*; Springer: Cham, Switzerland, 2014.
5. Robnik, M. Fundamental concepts of quantum chaos. *Eur. Phys. J. Spec.* **2016**, *225*, 959. [CrossRef]
6. Casati, G.; Chirikov, B.V.; Shepelyansky, D.L.; Guarneri, I. Relevance of classical chaos in quantum mechanics: The hydrogen atom in a monochromatic field. *Phys. Rep.* **1987**, *154*, 77. [CrossRef]

7. Bayfield, J.; Casati, G.; Guarneri, I.; Sokol, D. Localization of classically chaotic diffusion for hydrogen atoms in microwave fields. *Phys. Rev. Lett.* **1989**, *63*, 364. [CrossRef]
8. Prange, R.; Fishman, S. Experimental realizations of kicked quantum chaotic systems. *Phys. Rev. Lett.* **1989**, *63*, 704. [CrossRef]
9. Milburn, G.; Corney, J.; Wright, E.M.; Walls, D. Quantum dynamics of an atomic Bose-Einstein condensate in a double-well potential. *Phys. Rev. A* **1997**, *55*, 4318. [CrossRef]
10. Gardiner, S. (Quantum) chaos in Bose-Einstein condensates. *J. Mod. Opt.* **2002**, *49*, 1971. [CrossRef]
11. Mahmud, K.W.; Perry, H.; Reinhardt, W.P. Quantum phase-space picture of Bose-Einstein condensates in a double well. *Phys. Rev. A* **2005**, *71*, 023615. [CrossRef]
12. Li, S.C.; Pezzè, L.; Smerzi, A. Multiparticle entanglement dynamics of quantum chaos in a Bose-Einstein condensate. *Phys. Rev. A* **2021**, *103*, 052417. [CrossRef]
13. Huang, L.; Xu, H.Y.; Grebogi, C.; Lai, Y.C. Relativistic quantum chaos. *Phys. Rep.* **2018**, *753*, 1. [CrossRef]
14. Ying, L.; Lai, Y.C. Enhancement of spin polarization by chaos in graphene quantum dot systems. *Phys. Rev. B* **2016**, *93*, 085408. [CrossRef]
15. Gómez, J.; Kar, K.; Kota, V.; Molina, R.A.; Relaño, A.; Retamosa, J. Many-body quantum chaos: Recent developments and applications to nuclei. *Phys. Rep.* **2011**, *499*, 103. [CrossRef]
16. Bohm, D. A Suggested Interpretation of the Quantum Theory in Terms of "Hidden" Variables. I. *Phys. Rev.* **1952**, *85*, 166. [CrossRef]
17. Bohm, D. A Suggested Interpretation of the Quantum Theory in Terms of "Hidden" Variables. II. *Phys. Rev.* **1952**, *85*, 180. [CrossRef]
18. Holland, P.R. *The Quantum Theory of Motion: An Account of the de Broglie-Bohm Causal Interpretation of Quantum Mechanics*; Cambridge University Press: Cambridge, UK, 1995.
19. Pladevall, X.O.; Mompart, J. *Applied Bohmian Mechanics: From Nanoscale Systems to Cosmology*; CRC Press: Boca Raton, FL, USA, 2012.
20. Kocsis, S.; Braverman, B.; Ravets, S.; Stevens, M.J.; Mirin, R.P.; Shalm, L.K.; Steinberg, A.M. Observing the average trajectories of single photons in a two-slit interferometer. *Science* **2011**, *332*, 1170. [CrossRef] [PubMed]
21. Braverman, B.; Simon, C. Proposal to observe the nonlocality of Bohmian trajectories with entangled photons. *Phys. Rev. Lett.* **2013**, *110*, 060406. [CrossRef]
22. Foo, J.; Asmodelle, E.; Lund, A.P.; Ralph, T.C. Relativistic Bohmian trajectories of photons via weak measurements. *Nat. Comm.* **2022**, *13*, 4002. [CrossRef]
23. Wiseman, H. Grounding Bohmian mechanics in weak values and bayesianism. *N. J. Phys.* **2007**, *9*, 165. [CrossRef]
24. Iacomelli, G.; Pettini, M. Regular and chaotic quantum motions. *Phys. Lett. A* **1996**, *212*, 29. [CrossRef]
25. Frisk, H. Properties of the trajectories in Bohmian mechanics. *Phys. Lett. A* **1997**, *227*, 139. [CrossRef]
26. Makowski, A.; Pepłowski, P.; Dembiński, S. Chaotic causal trajectories: The role of the phase of stationary states. *Phys. Lett. A* **2000**, *266*, 241. [CrossRef]
27. Cushing, J.T. Bohmian insights into quantum chaos. *Phil. Science* **2000**, *67*, S430. [CrossRef]
28. Makowski, A.J.; Frackowiak, M. The simplest non-trivial model of chaotic causal dynamics. *Acta Phys. Pol. B* **2001**, *32*.
29. Wisniacki, D.A.; Pujals, E.R. Motion of vortices implies chaos in Bohmian mechanics. *Europhys. Lett.* **2005**, *71*, 159. [CrossRef]
30. Wisniacki, D.; Pujals, E.; Borondo, F. Vortex dynamics and their interactions in quantum trajectories. *J. Phys. A* **2007**, *40*, 14353. [CrossRef]
31. Santos Lima, H.; Paixão, M.; Tsallis, C. de Broglie–Bohm analysis of a nonlinear membrane: From quantum to classical chaos. *Chaos* **2024**, *34*, 023125. [CrossRef]
32. Contopoulos, G.; Tzemos, A.C. Chaos in Bohmian quantum mechanics: A short review. *Reg. Chaotic Dyn.* **2020**, *25*, 476. [CrossRef]
33. Gisin, N. Indeterminism in physics, classical chaos and Bohmian mechanics: Are real numbers really real? *Erkenntnis* **2021**, *86*, 1469. [CrossRef]
34. Efthymiopoulos, C.; Kalapotharakos, C.; Contopoulos, G. Nodal points and the transition from ordered to chaotic Bohmian trajectories. *J. Phys. A* **2007**, *40*, 12945. [CrossRef]
35. Efthymiopoulos, C.; Kalapotharakos, C.; Contopoulos, G. Origin of chaos near critical points of quantum flow. *Phys. Rev. E* **2009**, *79*, 036203. [CrossRef]
36. Tzemos, A.C.; Efthymiopoulos, C.; Contopoulos, G. Origin of chaos near three-dimensional quantum vortices: A general Bohmian theory. *Phys. Rev. E* **2018**, *97*, 042201. [CrossRef] [PubMed]
37. Tzemos, A.C.; Contopoulos, G. Unstable Points, Ergodicity and Born's Rule in 2d Bohmian Systems. *Entropy* **2023**, *25*, 1089. [CrossRef] [PubMed]
38. Borondo, F.; Luque, A.; Villanueva, J.; Wisniacki, D.A. A dynamical systems approach to Bohmian trajectories in a 2D harmonic oscillator. *J. Phys. A* **2009**, *42*, 495103. [CrossRef]
39. Parmenter, R.H.; Valentine, R. Deterministic chaos and the causal interpretation of quantum mechanics. *Phys. Lett. A* **1995**, *201*, 1. [CrossRef]
40. Horodecki, R.; Horodecki, P.; Horodecki, M.; Horodecki, K. Quantum entanglement. *Rev. Mod. Phys.* **2009**, *81*, 865. [CrossRef]
41. Zander, C.; Plastino, A. Revisiting Entanglement within the Bohmian Approach to Quantum Mechanics. *Entropy* **2018**, *20*, 473. [CrossRef]

42. Rosenbluth, M.; Sagdeev, R.; Taylor, J.; Zaslavski, G. Destruction of magnetic surfaces by magnetic field irregularities. *Nucl. Fus.* **1966**, *6*, 297. [CrossRef]
43. Contopoulos, G. Resonance phenomena and the non-applicability of the "third" integral. In Proceedings of the "Les Nouvelles Méthodes de la Dynamique Stellaire", Besançon, France, 21–24 September 1966; Hénon, M., Nahon, F., Eds.; Editions du Centre National de la Recherche Scientifique: Paris, France, 1967.
44. Lakshmanan, M.; Rajaseekar, S. *Nonlinear Dynamics: Integrability, Chaos and Patterns*; Springer: Cham, Switzerland, 2012.
45. Hénon, M.; Heiles, C. The applicability of the third integral of motion: Some numerical experiments. *Astron. J.* **1964**, *69*, 73. [CrossRef]
46. Hénon, M. Numerical exploration of Hamiltonian systems. *Chaotic Behav. Determ. Syst.* **1983**, *36*, 53.
47. Fordy, A.P. Hamiltonian symmetries of the Henon-Heiles system. *Phys. Lett. A* **1983**, *97*, 21. [CrossRef]
48. Fordy, A.P. The Hénon-Heiles system revisited. *Physica D* **1991**, *52*, 204. [CrossRef]
49. Nordholm, K.S.J.; Rice, S.A. Quantum ergodicity and vibrational relaxation in isolated molecules. *J. Chem. Phys.* **1974**, *61*, 203. [CrossRef]
50. Waite, B.A.; Miller, W.H. Mode specificity in unimolecular reaction dynamics: The Henon–Heiles potential energy surface. *J. Quant. Chem.* **1981**, *74*, 3910–3915. [CrossRef]
51. Takatsuka, K. Quantum chaos in the dynamics of molecules. *Entropy* **2022**, *25*, 63. [CrossRef] [PubMed]
52. Chattaraj, P.; Sengupta, S. Quantum fluid dynamics of a classically chaotic oscillator. *Phys. Lett. A* **1993**, *181*, 225. [CrossRef]
53. Sengupta, S.; Chattaraj, P. The quantum theory of motion and signatures of chaos in the quantum behaviour of a classically chaotic system. *Phys. Lett. A* **1996**, *215*, 119. [CrossRef]
54. Chattaraj, P.; Sengupta, S.; Poddar, A. Chaotic dynamics of some quantum anharmonic oscillators. *Cur. Sci.* **1998**, 74, 758.
55. Contopoulos, G.; Moutsoulas, M. Resonance cases and small divisors in a third integral of motion II. *Astron. J.* **1965**, *70*, 817. [CrossRef]
56. Merzbacher, E. *Quantum Mechanics*; John Wiley & Sons: New York, NY, USA, 1998.
57. Tzemos, A.C.; Contopoulos, G.; Efthymiopoulos, C. Bohmian trajectories in an entangled two-qubit system. *Phys. Scr.* **2019**, *94*, 105218. [CrossRef]
58. Tzemos, A.C.; Contopoulos, G. Ergodicity and Born's rule in an entangled two-qubit Bohmian system. *Phys. Rev. E* **2020**, *102*, 042205. [CrossRef]
59. Tzemos, A.; Contopoulos, G. The role of chaotic and ordered trajectories in establishing Born's rule. *Phys. Scr.* **2021**, *96*, 065209. [CrossRef]
60. Tzemos, A.C.; Contopoulos, G. A comparison between classical and Bohmian quantum chaos. *Chaos Sol. Fract.* **2024**, *188*, 115524. [CrossRef]
61. Gisin, N.; Percival, I.C. The quantum-state diffusion model applied to open systems. *J. Phys. A* **1992**, *25*, 5677. [CrossRef]
62. Breuer, H.P.; Petruccione, F. *The Theory of Open Quantum Systems*; Oxford University Press: New York, NY, USA, 2002.
63. Nassar, A.B.; Miret-Artés, S. *Bohmian Mechanics, Open Quantum Systems and Continuous Measurements*; Springer: Cham, Switzerland, 2017.